

# A Comparison of X-ray and Radio Emission from the Supernova Remnant Cassiopeia A

Jonathan W. Keohane<sup>1</sup>, Lawrence Rudnick<sup>2</sup> and Martha C. Anderson<sup>3</sup>

*The Department of Astronomy, The University of Minnesota  
116 Church St. SE, Minneapolis, MN 55455*

To appear in Volume 446 of  
*The Astrophysical Journal*  
August 1, 1996

## ABSTRACT

We compare the radio and soft X-ray brightness as a function of position within the young supernova remnant Cassiopeia A. A moderately strong correlation ( $r = 0.7$ ) was found between the X-ray emission (corrected for interstellar absorption) and radio emission, showing that the thermal and relativistic plasmas occupy the same volumes and are regulated by common underlying parameters. The logarithmic slope of the relationship,  $\ln(S_{\text{X-ray}}) = 1.2 \times \ln(S_{\text{radio}}) + \ln(k)$  implies that the variations in brightness are primarily due to path length differences. The X-ray and radio emissivities are both high in the same general locations, but their more detailed relationship is poorly constrained and probably shows significant scatter.

The strongest radio and X-ray absorption is found at the western boundary of Cas A. Based on the properties of Cas A and the absorbing molecular cloud, we argue that they are physically interacting.

We also compare ASCA derived column densities with  $\lambda 21$  cm H I and  $\lambda 18$  cm OH optical depths in the direction of Cas A, in order to provide an independent estimate of ISM properties. We derive an average value for the H I spin temperature of  $\approx 40^\circ K$  and measure the ratio OH/H<sub>2</sub>, which is nominally larger than previous estimates.

*Subject headings:* ISM: clouds, atoms, molecules, supernova remnants, individual: Cas A — radio lines: ISM — X-rays: ISM — radio continuum: ISM

---

<sup>1</sup>present address: Code 662, NASA/GSFC, Greenbelt, MD 20771; E-mail: jonathan@lheamail.gsfc.nasa.gov

<sup>2</sup>E-mail: larry@mazel.spa.umn.edu

<sup>3</sup>present address: Dept of Soil Science, University of Wisconsin, 1525 Observatory Drive, Madison WI 53706; E-mail: anderson@bob.soils.wisc.edu

## 1. Introduction

The basic hydrodynamical structure of idealized young supernova remnants (SNRs) seems well-understood from a theoretical standpoint (Gull 1973a, Chevalier 1982). We expect to find an outer shock, a contact discontinuity between the shocked circumstellar medium and the ejecta, and a reverse shock moving into and decelerating the ejected material. Each of these should give rise to radio and X-ray radiation, with different emissivities depending on the local physical processes.

Observationally, the situation is far from this ideal. In the best studied young SNR, Cas A, none of these structures can be clearly identified (Anderson & Rudnick 1995, hereafter A&R). There are also questions about the nature of the outer shock, where the expected tangential magnetic fields are not seen (e.g., Kepler - Dickel et al. 1989, and Tycho - Dickel et al. 1991). Inhomogeneities on a variety of scales also complicate the observational as well as the theoretical pictures (e.g. Borkowski et al. 1992, Cliffe & Jones 1994, Jun & Norman 1994).

We need to clarify the nature of actual SNR structures both to understand the hydrodynamics and also to begin addressing important physical issues such as magnetic field amplification and relativistic particle acceleration. Although reasonable theoretical mechanisms exist for these processes (Gull 1973b, Reynolds & Ellison 1992), the observational signatures are far from clear (e.g. Anderson et al. 1994). One fruitful approach to addressing such questions may be a careful examination of the relationship between the X-ray and radio emissivities within a remnant, because of the different physical processes involved.

The bulk of the X-ray emission at low energies results from thermal line emission (Becker et al. 1979, Holt et al. 1994, hereafter HGTN), depending primarily on the temperature ( $\approx 3$  keV) and density ( $\approx 10 \text{ cm}^{-3}$ ) of the plasma carrying most of the mass and momentum (Fabian et al. 1980, hereafter F80). On the other hand, the radio emission is synchrotron radiation from relativistic electrons ( $\epsilon \approx 0.05 - 8$  GeV) in magnetic fields of  $\approx 100 \mu\text{G}$  (Cowsik & Sarkar 1980). In one remnant, SN1006, X-ray synchrotron radiation is probably present at keV energies (Koyama et al., 1995), although this is an exceptional case.

Very little quantitative work has been done on the comparison of X-ray and radio emissivities in

SNRs. The canonical wisdom is that the two are well-correlated on large scales, but show little correlation at smaller spatial scales (F80, Matsui et al 1984, hereafter MLDG). MLDG studied these relations in Kepler, where they divided the remnant into twelve sectors and found a moderate correlation of the form  $\ln(S_{\text{X-ray}}) \approx (1.1 \text{ to } 2.5) \times \ln(S_{\text{radio}}) + \ln(\text{scale factor})$ .

We chose Cas A for study because of the availability of both high quality radio and X-ray data. In the cm wavelength range, Cas A is the brightest object in the sky outside of the solar system. At an age of 300 years, it is believed to be in a pre-Sedov phase, and is situated  $3.4^{+0.3}_{-0.1}$  kpc away (Reed et al. 1995), at the far edge of the Perseus arm. The column densities of hydrogen between here and Cas A ( $N_{\text{H}} \approx 10^{22} \text{ cm}^{-2}$ ) are such that the optical depths of 1-2 keV X-rays are of order unity. Therefore, column densities inhomogeneously distributed across the remnant, such as due to structures local to Cas A and the Perseus arm, can play a large role in determining the apparent soft X-ray morphology. For these same reasons, Cas A is an excellent choice as a background source for radio and X-ray interstellar medium (ISM) studies.

The ISM has been well-studied in  $\lambda 21$  cm absorption (Mebold and Hills 1975, hereafter MH75; Bieging et al. 1991, hereafter BGW; and Schwarz et al. 1996, hereafter SGK). Although BGW's VLA study was the highest resolution and most detailed, it only covered the velocity range of the Perseus arm. SGK's Westerbork study, though only at a resolution of  $30''$ , covered both the Orion and Perseus spiral arms. In addition there have been numerous molecular absorption studies using Cas A — in  $\text{H}_2\text{CO}$  (Goss et al. 1984), in CO (Troland et al. 1985, hereafter TCH and Wilson et al. 1993, hereafter WMMPO),  $\text{NH}_3$  (Batra et al. 1984 and Gaume et al. 1994) and OH (Bieging & Crutcher 1986, hereafter BC). The absorption patterns in the various *molecules* are similar to each other, but very different than that of the  $\text{H I}$ . However,  $\text{C II}$  seems to be correlated with the  $\text{H I}$  instead of the molecules (Anantharamaiah et al. 1994).

Rasmussen (1996, hereafter R96) studied the spatial dependence of X-ray model parameters using the ASCA satellite, resulting in a total column density ( $N_{\text{H}}$ ) map. In this paper, we compare the radio absorption data of BC and SGK to the  $N_{\text{H}}$  map of R96. From this we measure the scaling relation between column density and equivalent line widths from the radio absorption measurements of SGK and BC. This allows measurements of the average  $\text{H I}$  spin temper-

ature and the  $N_{\text{OH}}/N_{\text{H}_2}$  abundance of the ISM to be calculated.

## 2. Analysis

### 2.1. Comparing Cas A's X-ray and Radio Surface Brightnesses

In order to compare the HRI X-ray ( $S_{\text{HRI}}$ ) and radio ( $S_{\text{radio}}$ ) surface brightnesses, we must first correct for the soft X-ray optical depths, which are of order unity. The higher energy ASCA data do not suffer from this problem, but a full analysis of those data at sufficient resolution has not yet been done. In order to estimate the X-ray optical depths, we made use of BC's  $\lambda 18$  cm OH and SGK's  $\lambda 21$  cm H I absorption data (see Fig. 1 A & B and Fig. 2) to calculate the total column density ( $N_{\text{H}}$ , Fig. 1C and Fig. 2) of hydrogen along each line of sight to the remnant. Once an  $N_{\text{H}}$  map has been calculated, a corrected image of unabsorbed soft X-ray emission ( $S_{\text{X}_{\text{ctd}}}$ , Fig. 1E) can be derived. Next, we can compare the actual thermally produced X-ray surface brightness ( $S_{\text{X}_{\text{ctd}}}$ ) with Cas A's well-known radio synchrotron morphology ( $S_{\text{radio}}$ , Fig. 1F). We first describe a direct method for carrying out these corrections, and then the alternative scheme we found it necessary to use.

We start by writing the X-ray optical depth as

$$\tau_{\text{X}} \equiv \sigma_{\text{X}}^{\text{HRI}} \times N_{\text{H}} \quad (1)$$

where  $\sigma_{\text{X}}^{\text{HRI}}$  is the cross-section per hydrogen atom averaged over the HRI bandpass;  $N_{\text{H}}$  is the total number of hydrogen atoms along the line of sight. We can then calculate

$$N_{\text{H}} = N_{\text{HI}} + 2 \times N_{\text{H}_2} \quad (2)$$

For the atomic hydrogen,

$$N_{\text{HI}} = (1.83 \times 10^{18} \text{ } EW_{\text{HI}}) \left( \frac{T_{\text{spin}}}{\text{ } ^{\circ}\text{K}} \right) \text{ cm}^{-2} \quad (3)$$

where  $T_{\text{spin}}$  is the spin temperature of the atomic hydrogen, and the equivalent width in H I is calculated by integrating the observed optical depths  $\tau_v$  over all velocities

$$EW_{\text{HI}} \equiv \int \tau_v \text{ dv} \quad (4)$$

In the case of the molecular hydrogen, for which direct measurements are not available, we can use the OH

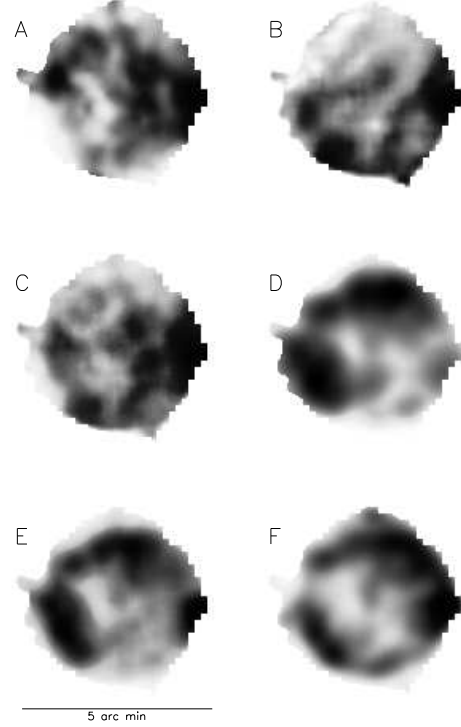


Fig. 1.—  $30''$  resolution images of Cas A. The histogram-equalization method of scaling was used to enhance the images. The quantities represented are: (A) the equivalent width of the  $\lambda 21$  cm line; (B) the equivalent width of the  $\lambda 18$  cm (OH) line; (C) the total column density as derived from images A and B; (D) the logarithm of the ROSAT HRI image; (E) the logarithmic HRI image corrected for absorption; (F) a logarithmic  $\lambda 20$  cm VLA continuum map. Histograms of the quantities shown in images A, B and C are shown in figure 2; image D ranges from  $-2.6$  –  $-0.8$   $\text{ln}(\text{cts s}^{-1} \text{ beam}^{-1})$ ; a plot of image E versus image F is shown in figure 4.

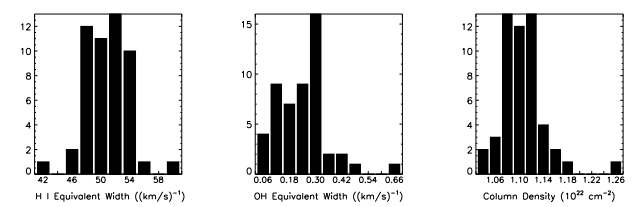


Fig. 2.— Histograms of  $\lambda 21$  cm equivalent width,  $\lambda 18$  cm equivalent width and the derived column density ( $N_{\text{H}} = D (EW_{\text{HI}}) + E (EW_{\text{OH}}) + F$ ).

absorption data, and write

$$N_{\text{H}_2} = \frac{N_{\text{H}_2}}{N_{\text{OH}}} \times (2.2 \times 10^{14} \text{ } EW_{\text{OH}}) \left( \frac{T_{\text{ex}}}{\text{ } ^\circ\text{K}} \right) \text{ cm}^{-2} \quad (5)$$

with equivalent width defined as above.

This approach (of finding the X-ray absorbing column densities *a priori* from radio line data) is the straight forward one, but it has several problems because of uncertainties in the scaling constants that must be used. The effective X-ray cross-section has been modeled by Morrison and McCammon (1983, hereafter M&M), who showed that the monoenergetic cross section depends strongly on photon energy and changes discontinuously at quantum thresholds. Therefore,  $\sigma_x^{\text{HRI}}$  is highly dependent on Cas A's soft X-ray spectrum, and thus has significant uncertainties. In addition, it is difficult to know what value to use for the H I spin temperature, as was demonstrated by MH75. Another major uncertainty comes from the OH abundance value. These issues will be discussed more fully in section 2.2.

We therefore adopted a different approach, simultaneously determining the X-ray/radio relationship and the absorption corrections by minimizing the quantity

$$\chi^2 \equiv \frac{[\ln(S_{\text{X}_{\text{ctd}}}) - \eta \ln(S_{\text{radio}}) - \ln(k)]^2}{\sigma_{\text{X}_{\text{ctd}}}^2 + (\eta_{i-1} \times \sigma_{\text{radio}})^2} \quad (6)$$

with respect to the parameters  $\eta, A, B$ , and  $[C - \ln(k)]$ , where the logarithmic *corrected* X-ray image is given by:

$$\begin{aligned} \ln(S_{\text{X}_{\text{ctd}}}) &= \ln(S_{\text{HRI}}) + \tau_x \\ &= \ln(S_{\text{HRI}}) + A \times EW_{\text{HI}} \\ &\quad + B \times EW_{\text{OH}} + C. \end{aligned} \quad (7)$$

The parameter  $\eta$  measures the logarithmic scaling between the X-ray and radio emission. The parameter  $[C - \ln(k)]$  contains both information on the normalization of emissivities (equation 6, parameter  $\ln(k)$ ), as well as allowing for absorption that is not well-modelled by the H I and OH optical depths (equation 7, parameter  $C$ ). This could be due, e.g., to H I saturation, variations in  $T_{\text{spin}}$ , which are not reflected in X-ray absorption, and the likely existence of Orion Arm molecular gas outside of the BC measurements.

Because the errors in the data are a function of the radio and X-ray flux, it is important that the error images are included in the determination of  $\chi^2$  (equation 6).

As a simplifying procedure, we performed the fits iteratively, holding the errors fixed as propagated from the previous best fit parameters ( $A_{i-1}$ ,  $B_{i-1}$ , and  $\eta_{i-1}$ ):

$$\begin{aligned} \sigma_{\text{X}_{\text{ctd}}}^2 &= \sigma_{\ln(S_{\text{HRI}})}^2 + (A_{i-1} \times \sigma_{EW_{\text{HI}}})^2 \\ &\quad + (B_{i-1} \times \sigma_{EW_{\text{OH}}})^2. \end{aligned} \quad (8)$$

Prior to performing the  $\chi^2$  analysis, the maps were prepared as follows. In order to match the resolution of the H I data, we smoothed the OH line and continuum maps to a resolution of  $30''$ , before calculating the optical depths and equivalent widths. We also smoothed the epoch 1990 (3.4 ks live-time) ROSAT HRI image (obtained from the HEASARC public archive) and the epoch 1987  $\lambda 20$  cm VLA continuum map described by A&R, to  $30''$  resolution. Errors in each map were calculated using standard methods. The resulting maps contain 51 independent beams, and are shown in figure 1. Histograms of the radio absorption values are shown in figure 2.

The minimum value of  $\frac{\chi^2}{N}$  was 47, showing that there is a large amount of scatter still unaccounted for in the X-ray/radio relation. The number of degrees of freedom,  $N$ , coincidentally, also equals 47. In order to calculate 70% and 99% confidence limits  $(\delta_{X70}, \delta_{X99})$  for parameter  $X$ , we determined the value of

$$\chi^2(X \pm \delta_{X70, X99}) \equiv \chi_{\min}^2 \times (1.097, 1.542) \quad (9)$$

where  $\chi_{\min}^2$  is the global minimum value of  $\chi^2$ . Following Bevington & Robinson (1992), while parameter  $X$  is being varied, all other parameters are allowed to float to minimize  $\chi^2$  for that value of  $X$ . Figure 3 shows contour plots of the confidence levels, as a function of parameters  $A$  and  $B$ ,  $\eta$  and  $[C - \ln(k)]$ .

Figure 4 shows the correlation between the thermal X-ray emission  $\ln(S_{\text{X}_{\text{ctd}}})$  and radio synchrotron radiation ( $\ln(S_{\text{radio}})$ ). The best fit slope is  $\eta = 1.21 \pm 0.41$ , (70% confidence limit), with the error probably dominated by real scatter in the X-ray/radio relation. In section 3, we will discuss the competing effects of emissivity and path length that can contribute to such differences.

## 2.2. Interstellar Medium Parameters

In this section, we introduce a technique for determining physical parameters of the ISM. Although our results have large uncertainties, the method is useful in confirming previous estimates, and could be

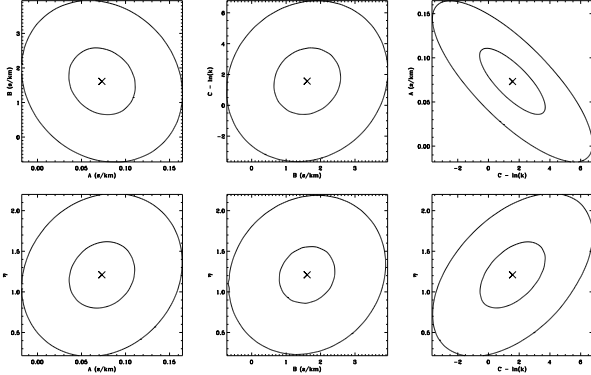


Fig. 3.— 70% and 99% confidence levels derived from the goodness of fit  $\chi^2$  obtained by fitting a power-law relation between the radio and corrected X-ray morphological distributions. They are shown here as a function of the parameters  $A$ ,  $B$ ,  $[C - \ln(k)]$  and  $\eta$  as defined in the text. The  $\times$  in each plot represents the minimum  $\chi^2$ .

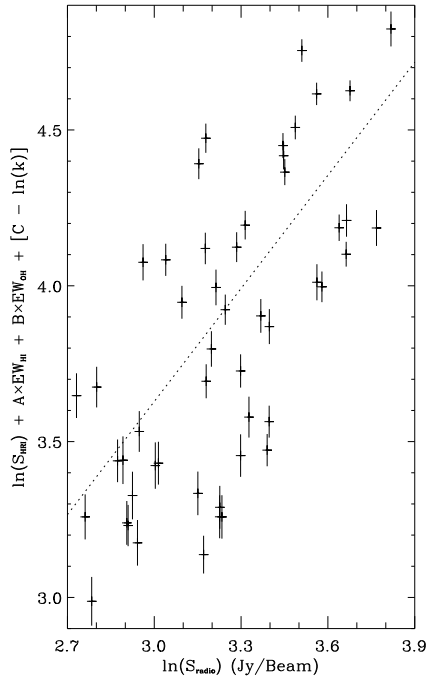


Fig. 4.— Plot of the logarithmic soft X-ray emission corrected for absorption using the best fit values for parameters  $A$ ,  $B$ , and  $[C - \ln(k)]$  as defined in equation 7 versus the logarithmic  $\lambda 20$  cm emission. The line represents our the best fit model:  $\ln(S_{X_{\text{ctd}}}) - \ln(k) = \eta \ln(S_{\text{radio}})$ .

extended to higher accuracy. Using the above procedure, we simultaneously determined the scaling parameters between H I and OH optical depths and soft X-ray absorption due to the line-of-sight ISM column density. The best fit values are  $A = 0.073 \pm 0.039$   $(\text{km/s})^{-1}$ ,  $B = 1.6 \pm 1.0$   $(\text{km/s})^{-1}$  and  $[C - \ln(k)] = 1.6 \pm 2.2$  (Fig. 3).

The X-ray absorption and the total column density can also be measured more directly through X-ray spectral fitting. With spectral fitting, the effective X-ray cross-section, which changes strongly as a function of photon energy (M&M), can be explicitly included. R96 assumed Cas A's X-ray spectrum to consist of power-law emission plus many Gaussian spectral emission lines (see HGTN), absorbed by the ISM assuming M&M's effective cross-sections. This resulted in a  $32 \times 32$  map ( $19''/\text{pixel}$ ) for each parameter fit, including the column density. A factor of 2 oversampling was used, so the “beam size” is approximately  $40''$ ; this is also a function of ASCA's complex point spread function (Tanaka et al., 1994). However, since these fits did not cover the whole image of Cas A, and because they rely on a “super-resolution” of the data, we chose not to use them for the original correction of the X-ray maps. We will, however, use the ASCA data to derive parameters of the interstellar medium.

In this section, we compare our optical depth image to R96's ASCA  $N_{\text{H}}$  image to derive a second set of scaling parameters for  $EW_{\text{HI}}$  and  $EW_{\text{OH}}$ . Combining this with the previously determined scaling parameters, and using equations 3 and 5, we can then determine both the effective ROSAT HRI cross section as well as some important ISM parameters.

To perform this analysis, we first aligned the ASCA field with our radio images by maximizing the cross-correlation of R96's  $N_{\text{H,ASCA}}$  image with our optical depth image ( $A \times EW_{\text{HI}} + B \times EW_{\text{OH}}$ ). This yielded a total of 25 independent  $30''$  beams with which to compare the X-ray and radio absorption. With  $N_{\text{H,ASCA}}$  in real physical units ( $10^{22} \text{ cm}^{-2}$ ) and the equivalent widths in km/s, we then minimized the quantity:

$$\chi^2(D, E, F) \equiv \sum (N_{\text{H,ASCA}} - N_{\text{H,radio}})^2 \quad (10)$$

where  $D$ ,  $E$ , and  $F$  are defined by

$$N_{\text{H,radio}} = D (EW_{\text{HI}}) + E (EW_{\text{OH}}) + F \quad (11)$$

The best fit values for parameters  $D$ ,  $E$  and  $F$  are:  $(7.1 \pm 3.8) \times 10^{-3}$ ,  $0.213 \pm 0.141$ , and  $0.69 \pm 0.19$  respectively (70% confidence); the  $\chi^2$  dependence on  $D$ ,  $E$ ,

and  $F$  is shown in Figure 5. The confidence limits are defined as:

$$\chi^2(X \pm \delta_{X70,X99}) \equiv (1.134, 1.831) \times \chi^2_{\min} \quad (12)$$

as appropriate for 22 degrees of freedom. The use of  $\chi^2_{\min}$  is necessary because R96 did not provide an error image.

At this point, we have two sets of scaling parameters for  $EW_{\text{HI}}$  and  $EW_{\text{OH}}$ . One set depends on the HRI cross section; the other does not. We can therefore use equations 7 and 11 to find that

$$\sigma_x^{\text{HRI}} = \frac{A}{D} = \frac{B}{E} \quad (13)$$

This yields  $\frac{A}{D} = 10.3 \pm 7.7$  and  $\frac{B}{E} = 7.6 \pm 6.8$  with a weighted average of  $\sigma_x^{\text{HRI}} = (8.8 \pm 5.1)$ ; all are in units of  $10^{-22} \text{ cm}^2$ . This value of  $\sigma_x^{\text{HRI}}$  is several times larger than the rough estimate we made by averaging the M&M cross-section values over the bandpass, weighted by the HRI effective area, and assuming a flat spectrum for Cas A. If this discrepancy is real, then it indicates that on average, Cas A's source spectrum is probably decreasing with increasing energy in the HRI bandpass.

From our measured parameters  $D$  and  $E$ , and assuming that we have isolated the contributions due to H I and OH in our  $\chi^2$  analysis, we can then use equations 3 and 5 and the values of  $D$  and  $E$  to calculate  $T_{\text{spin}}$  and  $N_{\text{OH}}/N_{\text{H}_2}$ . However, the presence of a significant non-zero value for  $F$  shows that we have not successfully modelled all of the X-ray absorption, and we will have to take this into account.

First, we consider the molecular hydrogen component. Figure 5 shows that there is very little correlation between parameter  $E$  and either parameter  $D$

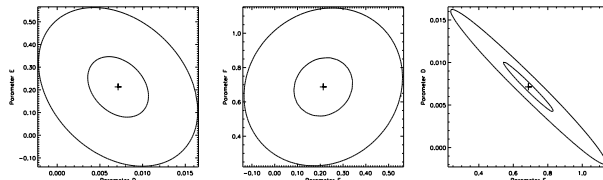


Fig. 5.— The  $\chi^2$  between the ASCA and radio absorption line derived column densities as a function of the scaling parameters  $D$ ,  $E$  and  $F$ , which are defined such that  $N_H = D (EW_{\text{HI}}) + E (EW_{\text{OH}}) + F$ . At each point in the plots, the parameter not shown was set to the value which would minimize  $\chi^2$  there. Contour levels represent confidence levels of 70% and 99%.

or  $F$ . This implies that our best fit parameter  $E$  is robust to uncertain contributions to the absorption from other ISM components. We therefore find the fraction of OH in the Perseus spiral arm as:

$$\frac{N_{\text{OH}}}{N_{\text{H}_2}} = (4.1 \pm 2.7) \times 10^{-6} \left( \frac{T_{\text{ex}}}{20^{\circ}\text{K}} \right). \quad (14)$$

This derived ratio is nominally higher than the  $(2.9 \pm 2.7) \times 10^{-7}$  quoted by WMMPO.

The contribution of the atomic component (parameter  $D$ ) is more problematic, because of its correlation with parameter  $F$  (see Fig. 5). Formally, we can calculate an average spin temperature for the H I as

$$T_{\text{spin}} = D / (1.83 \times 10^{-4}) = (39 \pm 21)^{\circ}\text{K}. \quad (15)$$

This temperature is the same as the spin temperature derived by Payne et al. (1994) towards Cas A and in the range of those found by Kalberla, et al. (1985), toward 3C147. The major contribution to the error in  $D$  actually comes from its correlation with  $F$ .

There are three likely sources for a non-zero  $F$ : Orion arm molecular gas (not measured by BC), saturated H I and hot intercloud H I.

TCH observed Orion arm  $^{13}\text{CO}$  column densities to be approximately 20% of the Perseus arm column density. This implies that only about  $6 \times 10^{20} \text{ cm}^2$  of  $N_{\text{HASCA}}$  ( $\approx 10\%$  of parameter  $F$ ) can be accounted for by molecular gas outside of BC's velocity range.

BGW named the highly saturated H I absorption feature near a velocity of -48 km/s "the curtain", because of its spatial uniformity and high optical depth (mostly above 5). Here SGK's H I equivalent width measurements underestimate the actual absorption. If SGK accounted for about half of the H I in "the curtain", the unmeasured portion should account for about  $1-2 \times 10^{21} \text{ cm}^2$  of  $N_{\text{HASCA}}$  or  $\approx 15\%$  of parameter  $F$ .

MH75 used the Effelsberg 100m telescope to observe the  $\lambda 21$  cm line in both emission and absorption toward Cas A. Their observations are consistent with a two-temperature H I model; where the hot component has spin temperatures in excess of about  $3500^{\circ}\text{K}$ , which would be observed only minimally by SGK (equation 3). MH75's estimated cloud/intercloud mass ratio is about 1:2, which could account for all of our measured parameter  $F$ .

These factors complicate our determination and interpretation of  $T_{\text{spin}}$ , as described above, so it should be considered simply as a characteristic value for the cooler gas.

### 3. Discussion

#### 3.1. The X-ray/Radio Emissivity Relation

The long-term objective of comparing the X-ray and radio emission in Cas A is to identify the state and structure of the thermal and relativistic plasmas and the physical connections between them. The X-ray emission spectrum from Cas A is itself believed to come from two different plasmas (Jansen et al. 1988). The low temperature plasma ( $kT < 1$  keV) is most likely reverse-shocked ejecta; models of the emission in the ROSAT band show that the emissivity is a mixture of thermal bremsstrahlung and line emission. The higher temperature plasma ( $kT \approx 3$  keV) is most likely circumstellar matter shocked by the blast wave. The reverse shock in Cas A is believed to currently dominate the soft X-ray emission (F80, Jansen et al.); the factors that influence the relative luminosity of these two shocks are discussed in detail by Masai (1994). We have shown here the importance of absorption for the low energy X-rays; analyses based on hardness ratios (e.g., HGTN) must first correct for this effect.

In the radio band, most of the emission comes from the bright ring, which is identified with either the reverse shock, the contact discontinuity, or both (Gull 1973 a, b). There is also a lower surface brightness radio plateau beyond the ring and a wealth of structures on smaller scales, including knots, bow shocks, filaments, etc, with lifetimes of order 30 years.

To interpret the observed radio/X-ray correlation, we must now distinguish between surface brightness and emissivity. If the emissivities in a remnant do not vary spatially, then all variations in surface brightness must be due to variations in path length (or filling factor), and the X-ray and radio brightnesses should be proportional to each other (logarithmic slope of 1). Some of the brightness variations in Cas A are clearly due to path length differences, such as the bright ring itself. However, even within the bright ring, the local radio brightness may largely be due to the path length through the emitting material at that position, rather than large variations in the intrinsic emissivity. The observations of Reed et al. (1995) show that the apparently complete Cas A shell is very non-uniform in optical line emission. The analysis of A&R show the presence of major dynamical asymmetries which are probably coupled to spatial variations. The large velocity gradients in the X-ray data from ASCA (HGTN) also demand large-scale non-spherical

structures in the X-ray emitting material.

Given the major role played by path length variations through the emitting material, our observed logarithmic slope of 1.2 for the X-ray/radio *surface brightness* relationship can be understood only as a lower limit to the slope relating the actual *emissivities*. If the variations in emissivity are much less than the variations in path length, the emissivity slope could be much higher. We are therefore unable to comment on how the various processes leading to soft X-ray and radio emission vary with one another. The same problem might easily affect the results of MLDG, whose X-ray/radio logarithmic slope could be as low as 1.1. At present, it is not clear how to isolate true variations in emissivity.

The modelling of the radio/X-ray emissivity relationship in an inhomogeneous rapidly-evolving remnant such as Cas A is also quite uncertain. It is important to avoid the simple scaling relations based on X-ray thermal bremsstrahlung, such as discussed by MLDG, because such relations ignore the dependence of line emission on factors other than density. In addition, we know from recent numerical simulations that the magnetic field amplification (Jun & Norman 1994) and relativistic particle acceleration (Jones et al. 1994) reflect the history of the plasma and cannot be simply described by current state parameters such as density and temperature. Jun (1995) has modeled the radio synchrotron radiation and the thermal bremsstrahlung component of X-ray emission in his 3D MHD simulations of young supernova remnants. Although he finds the same major features in the X-ray and radio emission, e.g., the clumpy bright ring, there is only a weak correlation between the two (Jun, 1996). This is due to the strong dependence of only the radio emission on the local magnetic field. Therefore, in order to effectively use such observations as presented here and in MLDG, we need both more sophisticated time-dependent analyses of the X-ray radiative transfer and an understanding of the relationship on various scales between the magnetic field and other hydrodynamical parameters.

#### 3.2. The Western Molecular Cloud

The western edge of Cas A is unusual in a number of ways, suggesting an interaction between the expanding SNR and a local molecular cloud. Considering the properties of Cas A itself, we first note that the brightest radio and X-ray emission is found in this region. HGTN show that the western region

has significantly lower X-ray equivalent widths than the other major emission regions. They interpret this as due to relatively stronger emission from the outer shock, which would be expected if it were moving into an area of higher density. A&R found that the motions of bright radio knots in the west showed extreme departures from the relatively uniform expansion seen in other regions. Many western knots are actually moving back toward the center of expansion - these must be due to an external interaction. This is also a region of steep radio spectral indices, implying that the conditions for relativistic particle acceleration are different here (Anderson & Rudnick, 1996).

On the opposite side of the remnant, there is a break in the shell, and groups of fast moving radio (A&R) and optical (Fesen et al., 1988) knots. This so-called “jet” could result from expansion into a lower density region opposite the molecular cloud. A similar situation is modelled by Tenorio-Tagle et al. (1985).

Turning now to the external material, figure 1 (image C) is the derived  $N_{\text{H}}$  map, which shows strong absorption on the western side of Cas A. This dense cloud also shows up as the extreme value in the column density histogram in Fig. 2. The cloud is at an LSR velocity of  $\approx -40$  km/s, placing it in the Perseus arm (Batra et al. 1984, Goss et al. 1984, TCH, BC and WMMPO). The OH column density maps of BC around -40 km/s trace out the regions of anomalous radio knot velocities and steep spectral indices discussed above. A trace of this cloud may also be visible in the H I measurements of BGW and SGK.

Gaume et al. (1994) studied the  $\text{NH}_3$  and CO absorption towards the bright western region. For the -39 km/s cloud, they determined the density to be  $n_{\text{H}_2} \approx 1000 \text{ cm}^{-3}$  characteristic of dark dust clouds, but found a higher than average kinetic temperature ( $\approx 18 \text{ }^{\circ}\text{K}$ ) and line width (3.5 km/s). They suggested that the high temperature could be due to either an increased level of cosmic rays, or by cloud-cloud collisions. On the basis of both the unusual properties of Cas A in the west and the unusual cloud conditions there, it thus seems quite likely that an interaction is currently in progress.

Wilson and Mauersberger (1994) pointed out that the circular shape of Cas A argues for a lack of external interaction. However, the bright radio ring illuminates material that has just recently been decelerated, because it is found in the same area as the optical fast moving knots, which are travelling several times faster (A&R). R. Dohm-Palmer & T.W. Jones

(1996) have performed 2D numerical simulations of an SNR expanding into a sharp ISM gradient. They find that at the time when the reverse shock on the high density side has reversed the velocity of some compact features, the overall ring deviates from being circular only by  $\approx 10\%$ . This is the same degree of non-circularity observed for Cas A’s bright ring, and so removes this objection to an external interaction.

#### 4. Conclusion

In this paper we have presented a technique to correct for spatially inhomogeneous absorption of soft X-rays in Cas A using radio absorption data. We find a good correlation between the soft X-ray and radio synchrotron emission from Cas A, but with significant scatter. The correlation is probably dominated by variations in path length, implying that the X-ray and radio emissions both occupy the same volumes. However, we have no evidence for a more detailed relation between their emissivities. A quantitative interpretation of these results requires more sophisticated modeling of both the X-ray radiative transfer and the relativistic plasma evolution in young SNRs.

Future X-ray/radio comparisons of Cas A should concentrate in at least the following two directions: studies at higher spatial resolution with deeper HRI measurements and comparisons with ASCA’s spatially resolved spectroscopy. With a deeper ROSAT HRI observation, it may be possible to separate emissivity from path length variations. In addition, X-ray proper motions could be measured and compared with the radio proper motions. Since HGTN’s paper, Cas A has been used as a calibrator for ASCA, so more ASCA data have been obtained and ASCA’s response functions have been refined. This will enable image reconstruction techniques to be applied to narrower bandpass images and better quality spatially resolved spectral fitting. Studying the correlations between the radio and X-ray morphologies as a function of X-ray energy will allow the different emission mechanisms and temperature and metalicity structures to be distinguished.

We have shown that Cas A is likely to be interacting with a dense cloud in the west. This has affected both the properties of the remnant and the cloud. Such interactions may play an important role both in SNR dynamics, and in the transfer of energy into the ISM.

We have also demonstrated a new technique for

probing the ISM. By comparing X-ray and radio spectroscopic absorption measurements, the H I spin temperature and molecular abundances ratios were measured. Future studies of other radio and X-ray bright extended objects can significantly enhance our understanding of the ISM, by comparing spatially resolved column densities from either the ROSAT PSPC or ASCA with radio and far IR atomic and molecular line data.

This work was supported in part by the National Science Foundation, through grant number AST 93-18959 to the University of Minnesota. Funding was also provided by NASA/GSFC's Laboratory for High Energy Astrophysics through the Graduate Student Researchers Program. This research has made use of data obtained from the US ROSAT Public Data Archive which is jointly managed by the ROSAT Science Data Center and the HEASARC. The HEASARC is a collaboration of the Laboratory for High Energy Astrophysics and the NSSDC at NASA/GSFC. The following data were kindly provided for our analysis — OH absorption data, John Bieging; ASCA column densities, Andrew P. Rasmussen; Westerbork H I absorption data, W. Miller Goss. We are also grateful for Goss's critical contributions as referee of this paper, and to John Dickey, B.I. Jun, Robert Petre and Ulrich Schwarz for helpful discussions and comments.

## REFERENCES

Anantharamaiah, K.R., et al., 1994, *ApJ*, 430, 682

Anderson, M.C., Jones, T.W., Rudnick, L., Tregillis, I.L. & Kang, H., 1994, *ApJ*, 421, L31

Anderson, M.C. & Rudnick, L., 1995, *ApJ*, 441, 307 (A&R)

Anderson, M.C. & Rudnick, L., 1996, *ApJ*, 456, 234

Batrla, W., Walmsley, C.M. & Wilson, T.L., 1984, *A&A*, 136, 127

Becker, et al., 1979, *ApJ*, 234, L73

Bevington, P.R. & Robinson, D.K., *Data Reduction and Error Analysis in the Physical Sciences* 2nd ed., ©1992, McGraw-Hill Inc.

Bieging, J.H., & Crutcher, R.M., 1986, *ApJ*, 310, 853 (BC)

Bieging, J.H., Goss, W.M. & Wilcots, E.M., 1991, *ApJS*, 75, 999 (BGW)

Borkowski, K.J., Blondin, J.M. & Sarazin, C.L., 1992, *ApJ*, 400, 222

Chevalier, R.A., 1982, *ApJ*, 259, 302

Cliffe, J.A. & Jones, T.W., 1994, *BAAS*, vol. 26, no. 2, p. 927, poster 41.07

Cowsik, R. & Sarkar, S., 1980, *MNRAS*, 191, 855

Dickel, J.R., Eilek, J.A., Jones, E.M. & Reynolds, S.P., 1989, *ApJS*, 70, 497

Dickel, J.R., van Breugel, W.J.M. & Strom, R.G., 1991, *AJ*, 101, 2151

Dohm-Palmer, R. & Jones, T.W., 1996, *ApJ*, submitted

Fabian, A.C., Willingale, R., Pye, J.P., Murray, S.S. & Fabbiano, G., 1980, *MNRAS*, 193, 175 (F80)

Fesen R.A., Becker, R.H. & Goodrich, R.W., 1988, *ApJ*, 329, L89

Gaume, R.A., Wilson, T.L. & Johnston, K.J., 1994, *ApJ*, 425, 127

Goss, W.M., Kalberla, P.M. and Dickel, H.R., 1984, *A&A*, 139, 317

Gull, S.F., 1973 *MNRAS*, 161, 47 (a)

Gull, S.F., 1973 *MNRAS*, 162, 135 (b)

Holt, S.S., Gotthelf, E.V., Tsunemi, H. & Negoro, H., 1994, *PASJ*, 46, L151 (HGTN)

Jansen, F.A., et al., 1988, *ApJ*, 331, 949

Jones, T.W., Kang, Hyesung & Tregillis, I.L., 1994, *ApJ*, 432, 194

Jun, B.I. & Norman, M.L., 1994, *BAAS*, vol. 26, no. 2, p. 925, poster 40.17

Jun, B.I., 1995, Ph.D. Thesis, University of Illinois

Jun, B.I., 1996, *private communication*

Kalberla, P.M.W., Schwarz, U.J. & Goss, W.M., 1985 *A&A*, 144, 27

Koyama, K., Petre, R., et al., 1995, *Nature*, 378, 255

Masai, K., 1994, *ApJ*, 437, 770

Matsui, Y., Long, L., Dickel, J. & Greisen, E., 1984, *ApJ*, 287, 295 (MLDG)

Mebold, U. & Hills, D.L., 1975, *A&A*, 42, 187 (MH75)

Morrison, R. & McCammon, D., 1983, *ApJ*, 270, 119 (M&M)

Payne, H.E., Anantharamaiah, K.R. & Erickson, W. C. 1994, *ApJ*, 430, 690

Rasmussen, A.P., 1996, *in preparation* (R96)

Reed, J.E., Hester, J.J., Fabian, A.C. & Winkler, P.F., 1995, ApJ, 440, 706

Reynolds, S.P. & Ellison, D.C., 1992, ApJ, 399, L75

Schwarz, U.J., Goss, W.M. & Kalberla, P.M.W., 1996, A&AS, submitted (SGK)

Tanaka, Y., Inoue, H. & Holt, S.S., 1994, PASJ, 46, L37

Tenorio-Tagle, G., Bodenheimer, P. & Yorke, H.W., 1985, A&A, 145, 70

Troland, T.H., Crutcher, R.M. & Heiles, C., 1985, ApJ, 298, 808 (TCH)

Wilson, T.L., et al., 1993, A&A, 280, 221 (WMMPO)

Wilson, T.L. & Mauersberger, R., 1994, A&A, 282, L41